# Phase-Shifting Full-Field Interferometric Methods for In-Plane Tensorial Stress Determination for Fracture Studies

Thesis by

Sharlotte Lorraine Bolyard Kramer

In Partial Fulfillment of the Requirements

for the Degree of

Doctor of Philosophy

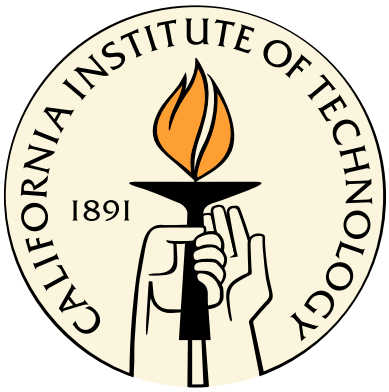


California Institute of Technology

Pasadena, California

2009

(Defended April 15, 2009)

To my family, friends, and Heavenly Father who give me strength.

# Acknowledgments

I would like to begin my acknowledgements with my two advisors, Guruswami (Ravi) Ravichandran and Kaushik Bhattacharya, for their practical and moral support during my five years at Caltech. This dynamic advising duo helped me navigate the sometimes treacherous waters of the Ph.D. thesis, always with some form of encouragement or useful prodding to get me to the finish. Ravi's advice to "just do it" and to "go for it" was not always easy for me, but usually proved to be the best medicine for a problem. Kaushik's enthusiasm for my progress kept my spirits up. They gave me the freedom to work through problems without letting me lose track of the goals of my thesis.

I must acknowledge Ares Rosakis for his enthusiasm for my research that combines two of his pet experimental methods and for this professional encouragement towards the end of my time at Caltech. I would like to acknowledge the remaining members of my thesis committee, Nadia Lapusta, Chiara Daraio, and Sergio Pellegrino, for their patience with schedules and for reading through my thesis that at first appears long, but is quite full of figures. I thank Eann Patterson of Michigan State University for his helpful discussions on photoelasticity. I would also like to thank my undergraduate advisor, Iaonnis Chasiotis, who still is a big professional support.

I must acknowledge the practical support of the National Defense Science and Engineering Graduate Fellowship program and the National Science Foundation Graduate Research Fellowship program. I would also like to acknowledge the National Science Foundation Center for the Science and Engineering of Materials at Caltech for their support of my research.

I also must acknowledge my friend and colleague, Michael Mello. He was responsible for teaching me the practical side of optics and has been a wonderful person to discuss theory with. He is a tremendous person to work with and be friends with. I would also like to acknowledge the members

of my research group who have been with me during the development of my research, providing helpful comments and camaraderie. I would like to acknowledge Linda Miranda for help with administrative issues and for her friendship. I must acknowledge the gentlemen of the Aeronautics Machine Shop for their practical help in making my parts and specimens, always with a smile.

In addition to the friends and colleagues I have already mentioned, I would like to acknowledge my many friends at Caltech that have been a great source of joy and strength, with special thanks to Sally Bane, Shannon Kao, Lydia Ruiz, Nathalie Vriend, and Sam Daly. I must also acknowledge my friends from afar, Emily Swafford and Crystal Cronan, who have helped me through it all over the phone and by email.

I must acknowledge my family: Mom, Dad, Philip, and Deborah. They have always encouraged me to work hard, strive to do well, and be a good person. Their love has been constant and unwavering. I also must thank my new family by marriage, Pat, Mike, Jason, Granny, and Grandpa, for their abundant enthusiasm and encouragement from across the globe in New Zealand.

I would like to state some special words of acknowledgement of my fabulous husband, Richard. He has been a constant rock to lean on during our entire time at Caltech, from homework sets to thesis writing. I can always trust in him for love, encouragement, practical help, a kind ear, and a hug. Even if I had not gained anything from my experience at Caltech other than him as a husband, I would still be eternally enriched and fortunate. The most important acknowledgement of them all is to God, my Lord and Savior. He has been the true foundation and source of strength of all that I do and all that I am. He has blessed me with many gifts. He presents me with challenges to teach me perseverance and hope in Him. All the glory must ultimately be given to Him.

# Abstract

Fracture criteria of anisotropic materials can be established with understanding of full-field stresses near a crack. The anisotropy of the stresses implies that the full in-plane tensorial stress is required, but current experimental optical techniques only give the sum or difference of principal stresses, motivating the development of an experimental method that combines two experimental techniques to determine all of the stress components. The proposed hybrid experimental method of phase-shifting photoelasticity and transmission Coherent Gradient Sensing (CGS) can determine the full-field in-plane tensorial stress around a crack. This thesis establishes this method for stress determination around cracks in photoelastic materials, the foundation for future studies extending this method to anisotropic materials.

The first step in developing this experimental method requires a new theory for the use of CGS, a wavefront shearing interferometry technique, for photoelastic materials. The first analysis and experimental verification of transmission wavefront shearing interferometry for photoelastic materials are presented. These interferometers applied to optically isotropic materials produce a single interference pattern related to one phase term, but when applied to photoelastic materials, they produce the sum of two different interference patterns with phase terms that are the sum and difference, respectively, of two stress-related phase terms. The two stress-related phase terms may be separated using phase shifting and polarization optics. These concepts are experimentally demonstrated using CGS in full field for a compressed polycarbonate plate with a side V-shaped notch with good agreement with theoretical data derived from Williams' solution for a thin plate with an angular corner. The analysis may be applied to any wavefront shearing interferometer by modifying parameters describing the wavefront shearing distance.

The new method that combines phase-shifting photoelasticity and transmission CGS is first developed to determine the tensorial stress field in thin plates of photoelastic materials. A six-step phase-shifting photoelasticity method determines principal stress directions and the difference of principal stresses. The transmission CGS method utilizes a standard four-step phase-shifting method to measure the $x$ and $y$ first derivatives of the sum of principal stresses. These stress derivatives are numerically integrated using a weighted preconditioned conjugate gradient (PCG) algorithm, which is also used for the phase unwrapping of the photoelastic and CGS phases. With full-field measurement of the sum and difference of principal stresses, the principal stresses may be separated, followed by the Cartesian and polar coordinate stresses using the principal stress directions and the polar angle. The method is demonstrated for in-plane tensorial stress determination for a compressed polycarbonate plate with a side V-shaped notch with good comparison to theoretical stress fields.

The CGS-photoelasticity experimental method is applied to determine stresses around Mode I-dominant cracks in Homalite-100. The cases presented here range in Mode I stress intensity factor, $K_I$, from about one-quarter to just below the fracture toughness and have small mode-mixity ratios $K_{II}/K_I$. This experimental method demonstrates the calculation of mode-mixity ratios as small as 0.0043 with a range of $-0.010$ to 0.020. The experimental stress fields have excellent agreement with the full-field 2D asymptotic crack solution using the $K_I$ and $K_{II}$ values calculated from the experimental data. With this foundation of stress determination around cracks in photoelastic materials and with some future analysis, this experimental method can be extended to determine stresses in anisotropic crystals for fracture studies.

# Contents

# List of Figures

# List of Tables

# Nomenclature

**Greek symbols**

| | | |
|---|---|---|
| $\alpha$ | isoclinic angle; angle of linear retardation of photoelastic material; angle between Cartesian and principal coordinate systems, Equation (3.3), Page 40 | radian |
| $\beta$ | angle of polarization axis of the second polarizer in the polariscope, Page 39 | radian |
| $\Delta h$ | thickness variation, Equation (2.5), Page 12 | m |
| $\Delta n_i$ | change in refractive index in the $i$-th direction, Equation (2.4), Page 12 | |
| $\Delta S_{1,2}$ | optical path difference along principal directions, Equation (2.6), Page 12 | |
| $\Delta S_a$ | general optical path difference along the $a$ axis, Equation (2.3), Page 11 | |
| $\delta$ | photoelastic isochromatic phase, Equation (3.1), Page 39 | radian |
| $\Delta\psi$ | wrapped phase difference between neighboring pixels, Equation (2.28), Page 32 | radian |
| $\epsilon$ | error associated with assumption relating CGS phases to derivatives of $\sigma_1 + \sigma_2$, Equation (4.7), Page 112 | |
| $\epsilon^{\delta}$ | error between experimental and theoretical $\delta$ for mixed-mode fracture, Equation (4.4), Page 84 | |
| $\epsilon^{\partial x}$ | error between experimental and theoretical $\varphi_{sum}^{\partial x}$ for mixed-mode fracture, Equation (4.4), Page 84 | |
| $\epsilon^{\partial y}$ | error between experimental and theoretical $\varphi_{sum}^{\partial y}$ for mixed-mode fracture, Equation (4.4), Page 84 | |

| | | |
|---|---|---|
| $\gamma$ | angle of $\pm 1$ diffraction relative to $z$ axis, Page 10 | radian |
| $\lambda$ | wavelength, Page 11 | m |
| $\lambda/2$ plate | half-wave plate | |
| $\lambda/4$ plate | quarter-wave plate | |
| $\lambda_o$ | exponent of $r$ in Williams asymptotic stress field, Page 23 | |
| $\mu_{SIF}$ | stress intensity factor ratio, Page 87 | |
| $\nu$ | Poisson's ratio | |
| $\omega$ | angular frequency of the electric field, Page 11 | |
| $\phi$ | angle of fast axis of the second $\lambda/4$ plate in the polariscope, Page 39 | radian |
| $\phi_{x,y}$ | arbitrary constant phase terms of $x$ and $y$ amplitudes of electric field, Page 11 | radian/s |
| $\rho$ | angle of polarization axis of first polarizer, Page 20 | radian |
| $\sigma_{\alpha\beta}$ | 2D stress components for Carteisian $\alpha, \beta = \{x, y\}$ or polar $\alpha, \beta = \{r, \theta\}$ | Pa |
| $\sigma_{\theta\theta}$ | hoop stress, Page 1 | Pa |
| $\sigma_{app}$ | far-field applied stress, Page 23 | |
| $\sigma_i$ | principal stress for $i = \{1, 2, 3\}$ | Pa |
| $\theta$ | polar coordinate for polar angle | |
| $\tilde{\Delta}$ | Ronchi grating separation, Page 10 | m |
| $\varphi$ | general phase of interference term, Equation (2.19), Page 17 | radian |
| $\varphi_{1,2}$ | phase of interference term for $I_{1,2}^{image}$, Equation (2.14), Page 15 | radian |
| $\varphi_{\alpha d}$ | compound phase related to $\alpha$ and $\phi_{diff}$, Equation (2.22), Page 18 | radian |
| $\varphi_c$ | phase of compound interference, Equation (2.17), Page 16 | radian |

| | | |
|---|---|---|
| $\varphi_{diff}$ | CGS phase related to $\sigma_1 - \sigma_2$, Equation (2.16), Page 16 | radian |
| $\varphi_{Ex}$ | phase of compound interference from pure $E_x\hat{\imath}$ input, Equation (2.22), Page 18 | radian |
| $\varphi_{Ey}$ | phase of compound interference from pure $E_y\hat{\jmath}$ input, Equation (2.23), Page 19 | radian |
| $\varphi_{sum}$ | CGS phase related to $\sigma_1 + \sigma_2$, Equation (2.16), Page 16 | radian |
| $\varphi_{sum}^{\partial x}$ | CGS phase related to the $x$ derivative of $\sigma_1 + \sigma_2$, Equation (4.3), Page 83 | radian |
| $\varphi_{sum}^{\partial y}$ | CGS phase related to the $y$ derivative of $\sigma_1 + \sigma_2$, Equation (4.3), Page 83 | radian |
| $\xi$ | angle of fast axis of first wave plate, Page 20 | radian |
| $\zeta$ | material remaining after angular corner removed, Page 23 | radian |
| $C_f$ | fitting coefficient for Williams asymptotic stress field, Page 23 | |

**Roman characters**

| | | |
|---|---|---|
| $A$ | absolute photoelastic constant, Equation (2.4), Page 12 | |
| $a$ | length of the side of the square base in a tetragonal crystal, Page 184 | Å |
| $A_o^{\pm 1}$ | nominal magnitude of pure $x$ or pure $y$ electric field amplitude after $\pm 1$ diffraction, Page 18 | |
| $a_1$ | length of straight notch in fracture specimens, Page 86 | m |
| $a_2$ | length of straight crack in fracture specimens, Page 86 | m |
| $A_o$ | nominal magnitude of pure $x$ or pure $y$ electric field amplitude, Page 18 | |
| $A_x$ | magnitude of $E_x$, Page 11 | |
| $A_x^{\pm 1}$ | magnitude of $x$ amplitude of $\boldsymbol{E}^{\pm 1}$, Page 14 | |
| $A_y$ | magnitude of $E_y$, Page 11 | |
| $A_y^{\pm 1}$ | magnitude of $y$ amplitude of $\boldsymbol{E}^{\pm 1}$, Page 14 | |
| $B$ | absolute photoelastic constant, Equation (2.4), Page 12 | |

| | | |
|---|---|---|
| $C$ | constant related to photoelasticity used in $\Delta S_{1,2}$, Equation (2.7), Page 13 | $m^2/N$ |
| $c$ | length of the long side of a tetragonal crystal, Page 184 | Å |
| $c_o$ | relative photoelastic (stress-optic) constant, Equation (3.1), Page 39 | $m^2/N$ |
| $d$ | depth of V-notch, Page 21 | |
| $d_{shear}$ | lateral shearing distance, Page 10 | m |
| $E$ | Young's (elastic) modulus | Pa |
| $E_1^{\pm 1}$ | amplitude in $\hat{p_1}$ direction of $\boldsymbol{E}^{\pm 1}$, Equation (2.11), Page 14 | |
| $E_2^{\pm 1}$ | amplitude in $\hat{p}_2$ direction of $\boldsymbol{E}^{\pm 1}$, Equation (2.11), Page 14 | |
| $E_1$ | amplitude for $\hat{p_1}$ direction of input electric field, Equation (2.9), Page 13 | |
| $e_1$ | rotational misalignment of input $\lambda/4$ plate, Page 43 | radian |
| $E_1^{image}$ | electric field amplitude in $\hat{p_1}$ direction at the image plane, Equation (2.11), Page 14 | |
| $E_2$ | amplitude for $\hat{p}_2$ direction of input electric field, Equation (2.9), Page 13 | |
| $e_2$ | rotational misalignment of output $\lambda/4$ plate, Page 43 | radian |
| $E_2^{image}$ | electric field amplitude in $\hat{p}_2$ direction at the image plane, Equation (2.11), Page 14 | |
| $e_3$ | rotational misalignment of output polarizer, Page 43 | radian |
| $E_x$ | $x$ amplitude of input electric field, Equation (2.1), Page 11 | |
| $E_x^{specimen}$ | $x$ amplitude of electric field after specimen, Equation (2.2), Page 11 | |
| $E_y$ | $y$ amplitude of input electric field, Equation (2.1), Page 11 | |
| $E_y^{specimen}$ | $y$ amplitude of electric field after specimen, Equation (2.2), Page 11 | |
| $g$ | constant related to photoelasticity used in $\Delta S_{1,2}$, Equation (2.7), Page 13 | |
| $G_{1,2}$ | Ronchi grating $1, 2$, Page 10 | |

$h$ nominal specimen thickness, Page 11 m

$h_d$ height of wrapped phase discontinuities, Page 17 radian

$I$ intensity (irradiance) of an interference pattern

$I^{circ}$ irradiance (intensity) at the image plane from circularly polarized electric field input, Equation (2.24), Page 19

$I_c^{circ}$ constant for compound interference pattern from circularly polarized electric field input depending on $I_o^{circ}$ and $\varphi_{diff}$, Equation (2.24), Page 19

$I_o^{circ}$ constant for compound interference pattern from circularly polarized electric field input, Equation (2.24), Page 19

$I^{Ex}$ irradiance (intensity) at the image plane from pure $E_x\hat{\imath}$ input, Equation (2.22), Page 18

$I_c^{Ex}$ constant for compound interference term for pure $E_x\hat{\imath}$ input depending on $I_o^{Ex}$, $\alpha$, and $\varphi_{diff}$, Equation (2.22), Page 18

$I_o^{Ex}$ constant for compound interference pattern for pure $E_x\hat{\imath}$ input, Equation (2.22), Page 18

$I^{Ey}$ irradiance (intensity) at the image plane from pure $E_y\hat{\jmath}$ input, Equation (2.23), Page 19

$I_c^{Ey}$ constant for compound interference term for pure $E_y\hat{\jmath}$ input depending on $I_o^{Ey}$, $\alpha$, and $\varphi_{diff}$, Equation (2.23), Page 19

$I_o^{Ey}$ constant for compound interference pattern for pure $E_y\hat{\jmath}$ input, Equation (2.23), Page 19

$I^{image}$ irradiance (intensity) of electric field at the image plane, Equation (2.12), Page 14

$I_1^{image}$ irradiance (intensity) of $E_1^{image}$, Equation (2.12), Page 14

$I_2^{image}$ irradiance (intensity) of $E_2^{image}$, Equation (2.12), Page 14

$I^{isotropic}$ irradiance (intensity) of CGS image for an isotropic material, Page 17

$I_{1o}$ constant in $I_1^{image}$ depending on $A_{x,y}^{\pm 1}$, $\alpha$ and $\phi_{x,y}$, Equation (2.16), Page 16

| | | |
|---|---|---|
| $I_{2o}$ | constant in $I_2^{image}$ depending on $A_{x,y}^{\pm 1}$, $\alpha$ and $\phi_{x,y}$, Equation (2.16), Page 16 | |
| $I_c$ | constant for compound interference term depending on $I_{1o}$, $I_{2o}$, and $\varphi_{diff}$, Equation (2.17), Page 16 | |
| $I_i$ | $i$-th phase-shifted image ($i = 1$–$6$ for photoelasticity, $i = 1$–$4$ for CGS) | |
| $I_o$ | constant in $I^{image}$, Equation (2.16), Page 16 | |
| $I_o$ | intensity (irradiance) of a photoelastic interference pattern, Equation (3.2), Page 39 | |
| $k$ | wave number, Page 11 | radian/m |
| $K_{Ic}$ | fracture toughness, Page 88 | MPa/$\sqrt{\text{m}}$ |
| $K_{II}$ | Mode II stress intensity factor, Equation (4.1), Page 82 | MPa$\sqrt{\text{m}}$ |
| $K_I$ | Mode I stress intensity factor, Equation (4.1), Page 82 | MPa$\sqrt{\text{m}}$ |
| $L$ | half of the CGS shearing distance, Page 181 | pixel |
| $L^f$ | height of image field of view, Page 15 | |
| $M_i$ | coefficients in intensity for polariscope with non-polarizing beamsplitter, $i = 1$–$4$, Equation (3.5), Page 42 | |
| $N$ | photoelastic fringe order, Equation (3.1), Page 39 | |
| $n_o$ | refractive index, Page 11 | |
| $p$ | pitch, i.e., line density of Ronchi grating, Page 10 | 1/m |
| $r$ | polar coordinate for radius | |
| $R_{x,y}$ | reflectance coefficients along the $\{x, y\}$ directions for a non-polarizing beamsplitter, Page 41 | |
| $s$ | sum of the in-plane principal stresses, Page 51 | |
| $t$ | time | s |

$T_{x,y}$ transmission coefficients along the $\{x, y\}$ directions for a non-polarizing beamsplitter, Page 41

$thresh$ user-defined threshold value used in correction of the wrapped isoclinic angle, Page 49

$w$ opening width of V-notch, Page 21

$W_i^{\delta}$ quality-driven weight function for PCG algorithm for the isochromatic phase for mixed-mode fracture at point $i$, Page 84

$W_i^{\partial x}$ quality-driven weight function for PCG algorithm for the CGS phase related to the $x$ derivative of $\sigma_1 + \sigma_2$ for mixed-mode fracture at point $i$, Page 84

$W_i^{\partial y}$ quality-driven weight function for PCG algorithm for the CGS phase related to the $y$ derivative of $\sigma_1 + \sigma_2$ for mixed-mode fracture at point $i$, Page 84

$W^f$ width of image field of view, Page 15

$x$ Cartesian coordinate

$y$ Cartesian coordinate

$z$ Cartesian coordinate

CGS Coherent Gradient Sensing, Page 10

FCT fast cosine transform, Page 29

G energy release rate, Page 1 N/m

NRMSD RMSD normalized by range of data, Page 32

PCG preconditioned conjugate gradient, Page 29

RMSD root mean square deviation, Page 32

**Sub-scripts and Super-scripts**

$()^{circ}$ related to circularly polarized electric field input

$()^{Ex}$ related to pure $E_x\hat{\imath}$ input

$()^{Ey}$ related to pure $E_y\hat{\jmath}$ input

$()^{image}$ refers to image plane

$()^{in}$ refers to input plane prior to specimen

$()^{resid}$ refers to residual stresses

$()^{specimen}$ refers to plane immediately after specimen

$()_c$ refers to a compound quantity

$()_p$ written in principal coordinate system

**Vectors and Matrices**

$\hat{\imath}$ $x$ direction unit vector

$\hat{\jmath}$ $y$ direction unit vector

$\hat{p}_i$ principal unit vectors for $i = \{1, 2, 3\}$, Equation (2.9), Page 13

$\mathbf{W}$ quality-driven weight function for PCG algorithm, Equation (2.28), Page 32

$\boldsymbol{E}_{\mathbf{(0,\pm 1)}}$ transmitted, then $\pm 1$ diffracted wavefront, Page 10

$\boldsymbol{E}_{\mathbf{(\pm 1,0)}}$ $\pm 1$ diffracted, then transmitted wavefront, Page 10

$\boldsymbol{E}^{\pm 1}$ once diffracted electric field vector after Ronchi gratings, Page 14

$\boldsymbol{E}_p^{image}$ electric field vector at the image plane, Equation (2.11), Page 14

$\boldsymbol{E}^{in}$ input electric field vector, Equation (2.1), Page 11

$\boldsymbol{E}_p^{in}$ input electric field vector in principal coordinates, Equation (2.9), Page 13

$\boldsymbol{E}_p^{specimen}$ electric field vector after the specimen in principal coordinates, Equation (2.10), Page 14

$\boldsymbol{f}(K_I, K_{II})$ function to be minimized by nonlinear least-squares fitting algorithm to determine $K_I$ and $K_{II}$, Equation (4.5), Page 85

# Chapter 1

# Introduction

Active materials that have coupled responses to external stimuli, such as ferroelectric crystals that exhibit electromechanical actuation and nonlinear optical properties, are advantageously used in applications such as actuators, microdevices, and photonics. In order to improve fabrication techniques that focus on making flat surfaces for these applications and to characterize device failure, their fracture properties need to be determined. Such materials undergo anisotropic fracture, but the criteria for anisotropic fracture are not well established. The commonly used fracture criteria from isotropic fracture mechanics of maximum Mode I stress intensity factor (max-$K_I$), zero Mode II stress intensity factor ($K_{II} = 0$), maximum hoop stress (max-$\sigma_{\theta\theta}$), and maximum energy release rate (max-$G$) lead to the same prediction of crack propagation path in isotropic materials, but not in anisotropic materials (Goldstein and Salganik, 1974; Cotterell and Rice, 1980; Hodgdon and Sethna, 1993; Azhdari and Nemat-Nasser, 1998). A set of theoretical numerical, and experimental studies of fracture in sapphire, a brittle anisotropic crystal, by Azhdari and Nemat-Nasser (1996, 1998) and Azhdari et al. (1998) determined that a stress-based fracture criterion best determines the crack kinking properties for this material. Such studies motivate determining anisotropic fracture criteria by knowledge of the anisotropic stress field around a crack tip, allowing for calculation of quantities such as $K_I$, $K_{II}$, $\sigma_{\theta\theta}$, and $G$, which may be compared to determine what best predicts the crack path and the critical conditions for crack initiation and propagation for a given anisotropic material.

In plane-stress problems for these materials, the anisotropy of the stress field implies that the sum or difference of the in-plane principal stresses is not sufficient to determine fracture properties,

as it is for linearly elastic isotropic materials. Therefore, the study of aniostropic fracture motivates the development of experimental methods employing full-field techniques to determine the full-field tensorial stress (i.e., $\sigma_{xx}$, $\sigma_{yy}$, and $\sigma_{xy}$) for fracture studies. This thesis presents the development and experimental validation of a hybrid experimental method of phase-shifting photoelasticity and transmission Coherent Gradient Sensing (CGS), a wavefront shearing interferometry technique, for full-field in-plane tensorial stress determination around cracks in photoelastic materials, which serves as the foundation for future work in extending this method for fracture studies in anisotropic crystalline materials.

## 1.1 Transmission Wavefront Shearing Interferometry for Photoelastic Materials

Wavefront shearing interferometry is a well-established optical technique for measuring many optical, material, and mechanical properties such as wavefront slope characterization (Murty, 1964), surface deformation (Park et al., 2003), and even fracture of materials (Tippur et al., 1991a,b; Rosakis, 1993; Krishnaswamy, 2000). Shearing interferometry essentially is the interference of a coherent wavefront with a copy of itself "sheared" or translated by a lateral distance $d_{shear}$; this technique is self-referencing and hence is insensitive to rigid body motion (Park et al., 2003; Tippur et al., 1991a,b; Rosakis, 1993). The general analysis of the interference pattern for standard wavefront shearing interferometers depends only on the wavefront characteristics and the distance $d_{shear}$. Once the parameters for producing the sheared wavefront and interfering the two wavefronts are characterized for a particular shearing method, then the analysis may be specified for that particular method. With several methods to produce the wavefront shearing, the choice of shearing interferometer depends on the requirements of the application, such as measurement sensitivity or compactness.

An important consideration to the analysis is how the wavefront is formed. For techniques that involve transmission through a material of interest, the shape and optical properties of the material are considered (e.g., spherical wavefront emanating from an optically isotropic plano-convex

lens.) In the case of a deformed material that is originally planar, thickness and refractive index variations in the material result in optical path differences that may be related to stresses. A general analysis of the optical path difference in this case has previously been completed for the method of caustics (Papdopoulos, 1993; Kobayashi, 1993; Shimizu et al., 1998). Though not a wavefront shearing interferometry technique, the method of caustics, which has been used for large stress gradient applications, does consider optical path differences due to a deformed material, resulting in a shadow spot in the far field. The method of caustics only gives a point measurement, which motivated the development of CGS that is capable of measuring full-field stress or displacement gradients when used in transmission or in reflection, respectively (Tippur et al., 1991a,b). CGS is a wavefront lateral shearing interferometer that achieves shearing by a pair of amplitude gratings; sensitivity adjustment is achievable through choice of grating line density, separation between the gratings, and light wavelength. Previously, CGS in transmission has been used only for optically isotropic materials (Tippur et al., 1991a,b; Krishnaswamy, 2000). CGS in reflection has been used for opaque isotropic materials (Tippur et al., 1991a,b), for materials with reflective coatings (Tippur et al., 1991a,b; Lee et al., 2001), and for composite materials (Rosakis, 1993; Liu et al., 1998). No previous studies have considered CGS in transmission for optically anisotropic materials.

Taking inspiration from the method of caustics applied to photoelastic materials, this study presents the first general analysis of an initially planar wavefront transmitted through a photoelastic material, in terms of electric field and optical path difference, for a general wavefront shearing interferometer; the analysis is then specifically applied to CGS. The analysis may easily be modified for any wavefront shearing interferometer by changing the experimental parameters related to the distance $d_{shear}$.

This study demonstrates that the resultant interference pattern is no longer a simple function of a single phase term related to the sum of principal stresses, denoted $\varphi_{sum}$, as in the case of optically isotropic materials. Due to the optical anisotropy from the stress birefringence, the interference patterns from the $x$ and $y$ coordinates of the electric field, $E_x$ and $E_y$, are no longer equivalent. Considering the interference patterns along the orthogonal principal axes of the photoelastic spec-

imen, denoted $I_1^{image}$ and $I_2^{image}$, the phase terms of these distinct interference patterns, $\varphi_1$ and $\varphi_2$, are $\varphi_{sum} + \varphi_{diff}$ and $\varphi_{sum} - \varphi_{diff}$, respectively, where $\varphi_{diff}$ is related to the difference of principal stresses. Thus, $\varphi_{diff}$ obscures the desired phase information, $\varphi_{sum}$, due to the optical anisotropy of the material. $\varphi_{diff}$ is zero for an optically isotropic material, and therefore is not an issue for isotropic materials. For a general incident electric field, wavefront shearing interferometry for photoelastic materials results in an image that is the superposition of $I_1^{image}$ and $I_2^{image}$, which is too complicated to analyze by itself. The desired phase $\varphi_{sum}$ may be recovered by using phase shifting and polarization optics. These concepts are demonstrated using CGS for a compressed polycarbonate thin plate with a V-shaped side notch with good agreement between experimental and theoretical data.

## 1.2 Experimental In-Plane Tensorial Stress Determination

The analysis of various complex geometries and materials requires the full-field measurement of the in-plane tensorial stress, but full-field optical interference techniques generally provide a linear combination of stress or strain components. For example, standard photoelasticity yields the difference of the principal stresses $(\sigma_1 - \sigma_2)$ and the principal directions, meaning the angle between the Cartesian and principal coordinate systems known as the isoclinic angle (Patterson et al., 1997; Siegmann et al., 2005). Coherent Gradient Sensing (CGS) in transmission, on the other hand, provides a spatial derivative of the sum of the principal stresses $(\sigma_1 + \sigma_2)$ when applied to thin plate specimens (Tippur et al., 1991a; Rosakis, 1993). Methods for the determination of the in-plane stress tensor often combine either one experimental technique with a theoretical or numerical analysis component or two experimental techniques. Among the single experimental and theoretical/numerical hybrid methods are photoelasticity and a shear difference method, which calculates stress components on a raster scan from initial values of stress determined by photoelastic parameters at the boundary points (Haake et al., 1996; Greene et al., 2007), a hybrid photoelasticity and finite element method technique (Berghaus, 1991), and a hybrid technique combining thermoelasticity, which relates to the change in the sum of principal stresses with surface temperature, and both theoretical and numerical

methods (Huang et al., 1990a,b). A double experimental hybrid technique utilizes reflection photoelasticity as a strain witness and thermoelasticity (Barone and Patterson, 1996; Sakagami et al., 2004); the opaque nature of photoelastic coatings in the infrared spectrum allows these techniques to investigate the same surface of the specimen (Greene et al., 2007; Barone and Patterson, 1998). Interferometric photoelasticity gives both the isochromatic phase, related to the difference of principal stresses, and the isopachic phase, related to the sum of principal stresses; these two fields may be separated using a Mach-Zehnder interferometer combined with a circular polariscope (Yoneyama et al., 2005).

In this study, the proposed technique combines two full-field optical techniques, CGS in transmission and photoelasticity, used simultaneously with the aid of phase-shifting diagnostics. The $x$ and $y$ derivatives from the CGS data are numerically integrated to provide the sum of principal stresses, which, when combined with the difference of principal stresses and principal stress directions derived from photoelasticity, yield full-field in-plane stresses in principal, Cartesian, or polar coordinate systems. This method is the most similar to interferometric photoelasticity, given that the sum and difference of principal stress fields both require phase shifting to extract phase information and that both techniques are used in transmission. The proposed technique differs from interferometric photoelasticity in that the sum of the principal stresses comes from stress gradient measurements. Additionally, the CGS optic parameters, as described in Chapter 2, may be varied to adjust the measurement sensitivity to optimize the fringe density. This study concentrates on the hybrid technique in transmission; further analysis would be required to determine if this method could be used in reflection, where the separation of the principal strains are considered. The use of this method in reflection would be similar to the combined reflection photoelasticity/thermoelasticity (Greene et al., 2007; Barone and Patterson, 1998), but in this case, a photoelastic coating would affect the displacement derivative measurement on the same surface using reflection CGS.

This study demonstrates the combined experimental techniques for polycarbonate, a linear elastic photoelastic material. The test configuration is a plate with a side V-shaped notch along the $-x$ axis, compressed uniformly along the $y$ axis. A six-step phase-shifting photoelastic method based on

Patterson et al. (1997) and Siegmann et al. (2005) utilizes a circular polariscope, except here a non-polarizing beamsplitter is positioned after the specimen to split the light such that the transmitted light travels through the remaining polariscope optics and the reflected light travels through the CGS optics. The photoelastic data involve two phases, the isoclinic angle $\alpha$ and isochromatic phase $\delta$, related to the principal stress directions and the difference of principal stresses, respectively. Phase shifting allows for the separation of these two phases, but produces "wrapped" data with a limited range due to inverse trigonometric functions. The wrapped isoclinic angle and isochromatic phase are both unwrapped using a global least square integration phase unwrapping algorithm called weighted preconditioned conjugate gradient (PCG) method (Ghiglia and Romero, 1994; Baldi et al., 2002). This robust method allows for discrete jumps in phase that may arise due to a free surface, imperative to studying specimens with cracks or cutouts.

Since a transmission CGS interference pattern for a photoelastic material is a superposition of two interference patterns, phase-shifting techniques combined with appropriate control of the input polarization state prior to the specimen, achieved by the first two optics of the circular polariscope, lead to the elimination of $\varphi_{diff}$, leaving the desired phase $\varphi_{sum}$. The remaining phase is unwrapped using the weighted PCG algorithm. The $x$ and $y$ derivatives of $\sigma_1 + \sigma_2$ from the CGS data from the vertical and horizontal shearing directions are integrated using the PCG algorithm as well. With the constant of integration identified by a boundary condition, the full-field sum and difference of principal stresses allow for separation of the principal stresses, which may be transformed into Cartesian or polar coordinate systems utilizing the isoclinic angle. Experimental data of the test problem shows good agreement with theoretical data generated from an asymptotic solution derived from Williams' (1952) solution for a thin plate with an angular corner.

## 1.3 Full-Field Experimental Methods for Fracture Studies

Having established the use of the proposed hybrid experimental method for full-field tensorial stress determination around a V-notch stress concentration in polycarbonate, the next stage in this study is to demonstrate the method for full-field tensorial stress determination around a crack in a pho-

toelastic material. To the author's knowledge, the only study of full-field tensorial stress determination in a cracked material is by Sakagami et al. (2004), who used thermoelasticity and reflection-photoelasticity applied to a mechanically loaded plate with a small central crack-like slit. This study determines the full-field stresses for an aluminum alloy plate 450 mm $\times$ 80 mm $\times$ 6 mm in dimension with a central crack-like slit through the thickness, 16mm in length and 0.2 mm in width. Their field of view is 200 mm $\times$ 80 mm centered around the slit. Although qualitative comparison of their full-field experimental tensorial stresses to their boundary element method simulation appears poor, they report less than 5% error in their $K_I$ calculation as compared to theory. The study by Sakagami et al. (2004) does demonstrate the capability for tensorial stress determination using their hybrid method for this situation, but for a large field of view, for a crack-like slit, and for an opaque isotropic material.

This thesis is intended to demonstrate full-field tensorial stress determination using the proposed hybrid transmission optical methods in photoelastic materials with an actual crack and for small fields of view around 4.6 mm $\times$ 4.6 mm, zoomed in very close around the crack. This study is the first to use a hybrid experimental method for full-field tensorial stress determination around cracks in photoelastic materials. The photoelastic material used here is Homalite-100, a brittle thermosetting polyester, often used as a model material for dynamic linear elastic fracture studies (Bradley and Kobayashi, 1971; Irwin et al., 1979; Dally, 1979; RaviChandar, 1982). Straight pre-cracks in the Homalite-100 specimens are loaded via a wedge opening load, which simulates Mode I loading. Four different load cases are presented, with calculated $K_I$ values ranging from about one-quarter to just below the fracture toughness, the critical value of $K_I$ for crack propagation, of Homalite-100. The experimental stress fields exhibit $K$-dominant stress behavior and show excellent comparison with the 2D asymptotic crack solution for mixed-mode fracture using the calculated $K_I$ and $K_{II}$ values from the experimental $\sigma_{xx}$ and $\sigma_{yy}$. The experimental stresses indicate that the wedge loading is not purely Mode I, but can have a slight Mode II component, with measured mode-mixity $K_{II}/K_I$ ranging from $-0.010$ to 0.020, demonstrating that this experimental method is sensitive enough to capture slight mixed-mode fracture. Since these cases are for small fields of view, these experimental

stress fields are for the local crack behavior, an important asset in studying small-scale specimens. The current method does have some known local error sources that can be improved, as will be discussed. This study of full-field tensorial stress determination around cracks in a photoelastic material lays the foundation for future research in extending this hybrid experimental method for determining fracture criteria in anisotropic crystals and in active materials like ferroelectric crystals.

## 1.4 Thesis Outline

This thesis is divided into four main chapters with a chapter for conclusions and three appendices of supporting derivations. Chapter 2 presents the first analytical derivation of transmission wavefront shearing interferometry applied to photoelastic materials and provides experimental verification of the theory using CGS as the specific wavefront shearing interferometry technique, based on Kramer et al. (2009a). Chapter 3 introduces six-step phase-shifting photoelasticity, describes how CGS and photoelasticity are combined experimentally and how the data is analyzed, and demonstrates the proposed phase-shifting full-field CGS-photoelasticty experimental method for in-plane tensorial stress determination in a compressed polycarbonate plate with a side V-notch, based on Kramer et al. (2009b). Chapter 4 demonstrates the proposed experimental method for in-plane tensorial stress determination around Mode I–dominant cracks in Homalite-100. Chapter 5 describes future improvements to the experimental method and possible extension of this method for fracture studies in anisotropic materials. Chapter 6 provides concluding remarks for the thesis. Appendix A presents the relationships between the principal, Cartesian, and polar in-plane tensorial stress components, as well as relevant derivatives of stresses. Appendix B derives the 2D stress field for a plate with a side V-notch under uniform normal loading used for the theoretical solution in the experimental verification studies in Chapters 2 and 3. Appendix C presents details on the theory of phase-shifting photoelasticity.